Research Article Vol. 33, No. 10 / 19 May 2025 / Optics Express 20573
Optics EXPRESS

Liquid-crystal adaptive equivalent q-plate device with tunable topological charge

María del Mar Sánchez-López,[1,2,*] Aleksandra Walewska,[3] Noureddine Bennis,[3] José Francisco Algorri,[4,5,6] Piotr Sobotka,[7,8] Marek Zyczkowski,[8] and Ignacio Moreno[1,9]

[1]Instituto de Bioingeniería, Universidad Miguel Hernández de Elche, 03202 Elche, Spain
[2]Departamento de Física Aplicada, Universidad Miguel Hernández de Elche, 03202 Elche, Spain
[3]Faculty of Advanced Technologies and Chemistry, Military Univ. Technology, 00-908 Warsaw, Poland
[4]Photonics Engineering Group, University of Cantabria, Santander 39005, Spain
[5]CIBER Bioingeniera, Biomateriales, Nanomedicina, Instituto de Salud Carlos III, 28029 Madrid, Spain
[6]Instituto de Investigación Sanitaria Valdecilla (IDIVAL), 39011 Santander, Spain
[7]Faculty of Physics, Warsaw University of Technology, 00-662 Warsaw, Poland
[8]Institute of Optoelectronics, Military University of Technology, 00-908 Warsaw, Poland
[9]Departamento de Ciencia de Materiales, Óptica y Tecnología Electrónica, Universidad Miguel Hernández de Elche, 03202 Elche, Spain
*mar.sanchez@umh.es

Abstract: In this work we present the proof-of-concept of what we believe to be a novel liquid-crystal compact and transmissive device useful to generate cylindrical vector beams (CVBs) of tunable topological charge. The device combines two adaptive spiral phase plates (ASPP) in orthogonal directions and a quarter-wave plate (QWP). Each ASPP relies on a specially designed circular transmission electrode with radial lines to generate a spiral phase upon addressing two voltages. The combination of two orthogonal ASPP allows imparting two independent spiral phases onto two orthogonal linear polarization states that are converted into circular states by the final QWP, thus efficiently realizing arbitrary CVBs. By adjusting the four addressed voltages, the topological charges can be tuned to provide pure or hybrid CVBs with arbitrary topological charges. The device performance is analyzed in terms of the mapping relations between the Poincaré sphere and the higher-order Poincaré sphere. We find that it performs as a q-plate, but with the remarkable advantage of providing dynamic control of the topological charge in vortices and CVBs. Hence, we name it adaptive q-plate (AQ-plate). Experimental results demonstrate the versatility of the device.

1. Introduction

Cylindrical vector beams (CVB), featuring and axially symmetric distribution of the phase and polarization in the beam's cross section have been a major topic in Optics in the last two decades [1]. They can be regarded as the superposition of two optical vortices with orthogonal polarizations. Hence, these beams exhibit helical wavefronts carrying orbital angular momentum (OAM) and an inhomogeneous local state of polarization. These unique properties make them very useful in applications that range from light trapping [2], singular optics [3], super-resolution imaging [4], or optical communications [5], among others. Many different techniques have been developed in these years for their generation. The most common methods are based either on the dynamic control of the phase by means of spatial light modulators (SLMs) or those based on geometric phase diffractive elements and structured materials. Those based on SLMs present the great advantage of being programmable [6,7] and can be combined with other optical functions to create parallel CVBs [8]. As drawbacks, SLMs introduce losses due to their pixelated structure,

#560620 https://doi.org/10.1364/OE.560620
Journal © 2025 Received 25 Feb 2025; revised 10 Apr 2025; accepted 15 Apr 2025; published 6 May 2025

Optics EXPRESS

they have a limited spatial resolution, and they require building bulky optical systems. By contrast, methods based on structured materials are very compact and very efficient. These are micro-structured retarders with an optical axis spatial distribution that encodes a target phase function. They have been produced with liquid-crystal (LC) materials [9–11], by femtosecond laser nano-structuring of glass [12], and more recently with metamaterials [13]. However, these are in most cases static elements whose performance parameters are set on fabrication. Consequently, they cannot provide a dynamic control of the generated CVB. Other techniques to generate CVBs combine one SLM with structured retarders, like the polarization-selective cylindrical lenses employed in [14].

One of the most popular elements for generating CVBs is the q-plate device introduced in 2006 by Marrucci *et al.* [15]. It is a geometric phase element whose optical axis spatial distribution follows q times the azimuthal angle (θ) in the plane of the device, thus encoding a spiral phase. It can be fabricated through LC photoalignment techniques to achieve the azimuthal patterning of the LC director [16]. This structure imparts a helical phase to one circular polarization component, and the opposite helical phase to the other circular polarization component. For half-wave retardance of the LC layer, the maximum polarization conversion efficiency is achieved, thus fully converting an input beam with uniform polarization into a CVB of order $\ell = 2q$. Since their invention, q-plates have proved very useful in applications involving the manipulation of optical vortices and vector beams [17–20]. Introduced in a cavity they have been useful to produce CVBs outputs directly from a laser [21]. In addition, LC devices can be made tunable if indium-titanium oxide (ITO) transparent electrodes are incorporated. Tunable LC q-plates have been reported [22–24], where their tunability refers exclusively to the capability of adjusting the retardance. This is very convenient since the LC retardance strongly depends on the wavelength of light. The q-plate performance is only optimal for those wavelengths fulfilling the half-wave retardance condition [25,26]. Thus, the capability of tuning the retardance of the LC layer allows operating the q-plate optimally at different wavelengths. However, the q value of these tunable LC q-plates (and therefore the order of the generated CVB) is set during the photoalignment process and cannot be tuned.

Q-plates are restricted to impart a spiral phase with integer topological charge of equal magnitude but opposite sign to each circular polarization component, thus creating pure CVBs whose polarization pattern does not change upon propagation and defines the higher-order Poincaré sphere (HOPS) [27]. However, they cannot produce the so-called hybrid CVBs, which have arbitrary charges in the circular polarization components and are represented on the hybrid HOPS [28]. An exception are detuned q-plates operated at quarter-wave retardance [24], which generate full Poincaré beams [29], useful to perform single shot polarimetry [30]. These are a particular case of hybrid CVBs with zero charge in one of the circular components while the entire topological charge is encoded in the orthogonal component. Generic hybrid CVBs can be created using the j-plate device [31,32], a recent extension of the q-plate that enables the independent encoding of topological charges on two orthogonal polarizations. The j-plate can be fabricated with metamaterials, but not with LC materials, thus not yet programmable. Of course, SLM-based systems allow the independent manipulation of the topological charges to generate arbitrary hybrid vector beams [33,34] but this is at the expense of bulkier and less efficient setups. In addition, because of their rectangular pixelated array, SLMs are not well adapted to display the continuous azimuthal phase required to generate CVBs. The SLM spatial resolution limits the reproduction of the spiral phase in the central part of the pattern.

In this work we introduce the proof-of-concept of a new device explicitly designed for creating CVBs that presents several advantages compared to the previous technologies. It is based on a recently demonstrated adaptive LC spiral phase plate (ASPP) featuring a customized distribution of the ITO electrodes [35]. The ASPP generates an azimuthal voltage distribution in the LC layer that yields the spiral phase required in a vortex plate. Compared to other LC devices useful to

Optics EXPRESS

generate a spiral phase with discrete phase steps [36,37], the ASPP generates continuous spiral phases with different topological charges that can be tuned by applying only two voltages. We build a compound device that combines two such novel ASPPs and a quarter-wave plate (QWP) to generate CVBs. The constituent ASPPs are now made of LC with higher birefringence compared to that in [35] ($\Delta n = 0.27$ at $\lambda = 633$ nm instead of $\Delta n = 0.16$), thus reaching larger topological charges ($\ell = \pm 12$ instead of $\ell = \pm 4$). The device is tunable, compact and highly efficient since, unlike SLMs, diffraction losses are non-significant. It can be operated at different wavelengths and allows to dynamically encode different topological charges simply by changing the voltage values. Since the spiral phases encoded in the orthogonal polarization states are independent, it is useful to generate both pure and hybrid CVBs. We name this compound device adaptive q-plate (AQ-plate).

The paper is organized as follows: after this introduction, Section 2 briefly reviews CVBs and describes how they can be produced. Then, Section 3 introduces the new device, the AQ-plate and its mode of operation. Section 4 presents experimental results. Namely, the verification of the spiral phase in the ASPP elements constituting the AQ-plate and the subsequent generation of pure and hybrid CVBs. Finally, in Section 5 the main conclusions of this work are provided.

2. Cylindrical vector beams and the higher-order Poincaré sphere

Figure 1(a) presents the standard Poincaré sphere (PS) that describes a fully polarized state as a unique point on the sphere surface. Any polarization elliptical state can be expressed as:

$$|\mathbf{e}\rangle = \cos(\chi)e^{-i\alpha}|\mathbf{R}\rangle + \sin(\chi)e^{i\alpha}|\mathbf{L}\rangle, \tag{1}$$

in the basis of the circular polarization states, $|\mathbf{R}\rangle$ and $|\mathbf{L}\rangle$, given by the Jones vectors:

$$|\mathbf{R}\rangle = \frac{1}{\sqrt{2}}\begin{pmatrix} 1 \\ +i \end{pmatrix}, \qquad |\mathbf{L}\rangle = \frac{1}{\sqrt{2}}\begin{pmatrix} 1 \\ -i \end{pmatrix}. \tag{2}$$

The angle χ, with $0 \leq \chi \leq \pi/2$, controls the relative magnitude between the circular components and defines the ellipticity angle as $\varepsilon = \pi/4 - \chi$. The angle 2α, where $0 \leq \alpha \leq \pi$, directly provides the azimuth of the polarization state. The latitude and the longitude coordinates on the sphere are given respectively by 2ε and 2α. Thus, the circular states are located on the poles and the linear states lie on the equator of the PS.

As mentioned, CVBs are light beams with a structured spatial pattern in their transversal plane that is axially symmetric; thus, following the azimuthal angle (θ). A common approximation [5] describes these beams as

$$|\mathbf{e}_{\ell_R,\ell_L}(\theta)\rangle = \cos(\chi)e^{i(\ell_R\theta-\alpha)}|\mathbf{R}\rangle + \sin(\chi)e^{i(\ell_L\theta+\alpha)}|\mathbf{L}\rangle. \tag{3}$$

Here ℓ_R and ℓ_L are the topological charges encoded, respectively, in the $|\mathbf{R}\rangle$ and $|\mathbf{L}\rangle$ states. Pure CVBs are obtained when $\ell_R = -\ell_L$. These states in Eq. (3) define the higher-order Poincaré sphere (HOPS) [27]. Figure 1(b) presents the first-order HOPS, where topological charges are $\ell_L = +1$ and $\ell_R = -1$. The two states located in the poles are circularly polarized vortex beams, while the states located on the equator ($\chi = \pi/4$) are linearly polarized CVBs (also named vortex vector beams), which include the radial $|\mathbf{Rd}\rangle$, the slanted $|\mathbf{Sl}\rangle$, the azimuthal $|\mathbf{Az}\rangle$ and the anti-slanted $|\mathbf{Asl}\rangle$ CVBs as particular cases for $2\alpha = 0, \pi/2, \pi$ and $3\pi/2$ respectively, i.e, having Jones vectors:

$$|\mathbf{Rd}\rangle = \begin{pmatrix} \cos(\theta) \\ \sin(\theta) \end{pmatrix}, |\mathbf{Az}\rangle = \begin{pmatrix} -\sin(\theta) \\ \cos(\theta) \end{pmatrix}, \tag{4a}$$

Optics EXPRESS

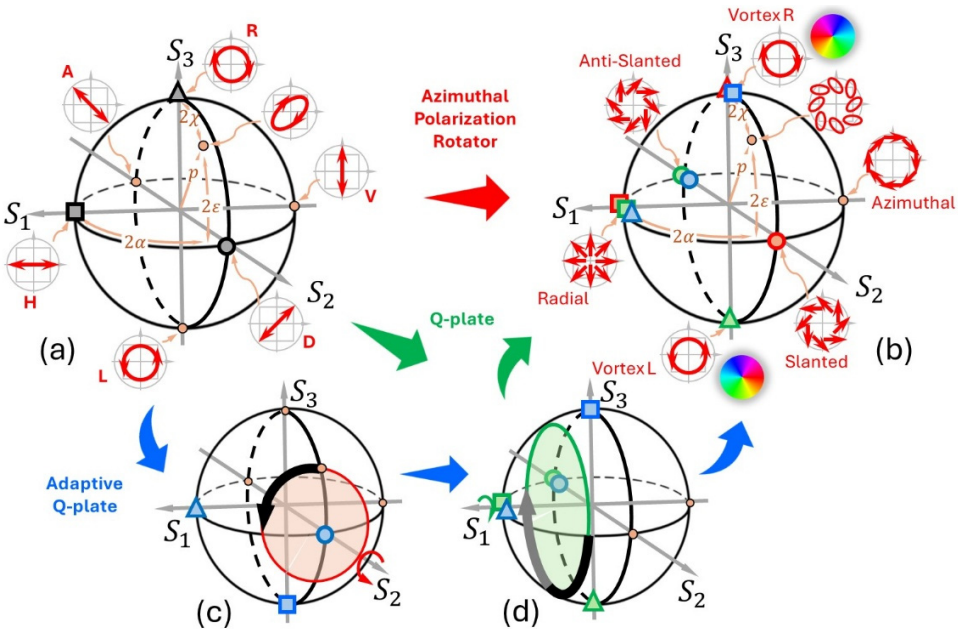

Fig. 1. (a) Poincaré sphere (PS) and (b) higher-order Poincaré sphere (HOPS) for CVB with $\ell_L = +1$ and $\ell_R = -1$. (c-d) Polarization transformations of the PS that provide the mapping to the HOPS for a q-plate (green arrows) and for an AQ-plate (blue arrows). The colour symbols (triangle, square, circle) in the HOPS (Fig. 1(b)) result from the action of the AQ-plate (blue symbols), the standard q-plate (green symbols) and the azimuthal polarization rotator (red symbols) on the input polarization state indicated with the corresponding symbol in the PS (Fig. 1(a)).

$$|\mathbf{Sl}\rangle = \begin{pmatrix} \cos\left(\theta + \frac{\pi}{4}\right) \\ \sin\left(\theta + \frac{\pi}{4}\right) \end{pmatrix}, |\mathbf{Asl}\rangle = \begin{pmatrix} \cos\left(\theta - \frac{\pi}{4}\right) \\ \sin\left(\theta - \frac{\pi}{4}\right) \end{pmatrix}. \tag{4b}$$

The radial $|\mathbf{Rd}\rangle$ and azimuthal $|\mathbf{Az}\rangle$ states are aligned along the S1 axis in the first-order HOPS, while the slanted $|\mathbf{Sl}\rangle$ and anti-slanted $|\mathbf{Asl}\rangle$ states lie along the S2 axis (Fig. 1(b)).

An azimuthal rotator, i.e. a device that rotates the input polarization by the azimuthal angle θ, is described by the following Jones matrix $\mathbf{T}$:

$$\mathbf{T} = e^{+i\theta}|\mathbf{L}\rangle\langle\mathbf{L}| + e^{-i\theta}|\mathbf{R}\rangle\langle\mathbf{R}| = \begin{pmatrix} \cos(\theta) & -\sin(\theta) \\ \sin(\theta) & \cos(\theta) \end{pmatrix}. \tag{5}$$

This device provides a direct mapping, with the same $(2\alpha, 2\varepsilon)$ coordinates, between the input polarization represented as a point on the standard PS and the output CVB represented on the HOPS. Such direct mapping is indicated by the red arrow in Fig. 1, and it also corresponds to the phase shifter device introduced in [14].

A q-plate performs additional polarization transformations that can be visualized as rotations of the PS prior to the direct mapping provided by the azimuthal rotator. The standard q-plate yielding first-order CVBs is a HWP whose principal axis rotates as $\theta/2$, and is defined by the Jones matrix $\mathbf{Q}$ [15]

$$\mathbf{Q} = e^{+i\theta}|\mathbf{L}\rangle\langle\mathbf{R}| + e^{-i\theta}|\mathbf{R}\rangle\langle\mathbf{L}| = \begin{pmatrix} \cos(\theta) & \sin(\theta) \\ \sin(\theta) & -\cos(\theta) \end{pmatrix}. \tag{6}$$

Optics EXPRESS

Note that this matrix can be decomposed as the product $\mathbf{Q} = \mathbf{T} \cdot \mathbf{H_w}$ [38], where $\mathbf{H_w} = |\mathbf{H}\rangle\langle\mathbf{H}| - |\mathbf{V}\rangle\langle\mathbf{V}| = \mathrm{diag}[1, -1]$ stands for the Jones matrix of a HWP aligned along the S1 axis. The matrix $\mathbf{H_w}$ induces a 180° rotation of the PS around the S1 axis (Fig. 1(d)), after which a direct mapping with equal coordinates is performed by the $\mathbf{T}$ matrix. Thus, the path indicated by the green arrows in Fig. 1 illustrates the mapping relations provided by the q-plate [39]. The proposed AQ-plate provides an additional transformation, illustrated with the blue arrows in Fig. 1, as it will be described in the next section.

When CVBs described by Eq. (3) are projected onto a linear analyzer, a scalar beam is obtained, in the sense that it has a uniform polarization. But the CVB polarization pattern can be retrieved from the shape of the transmitted intensity, which shows azimuthal lobes, in what is sometimes referred to as petal beams [40]. In the case of the first order HOPS, the projection onto the analyzer provides the states of the OAM Poincaré sphere [41,42]. Figure 2 shows some examples of $\ell_L = -\ell_R = 1,\ 2,\ 3$ and $\chi = \pi/4$, thus the CVBs are linearly polarized, and with $\alpha = 0$ and $\alpha = \pi/2$. For every example, the numerical simulations plotted on the left panels show the CVB intensity and polarization patterns. In all cases, the beam features a dark central spot created by the polarization singularity and the corresponding polarization map. For the first order CVBs, these angles correspond to the radial (a) and to the slanted (b) polarization. The right panels show the intensity of the CVB transmitted through a linear polarizer with diagonal orientation. Obviously, rotating the polarizer provokes a rotation of the lobes. We will make use of this effect to probe the generation of CVBs with the AQ-plate.

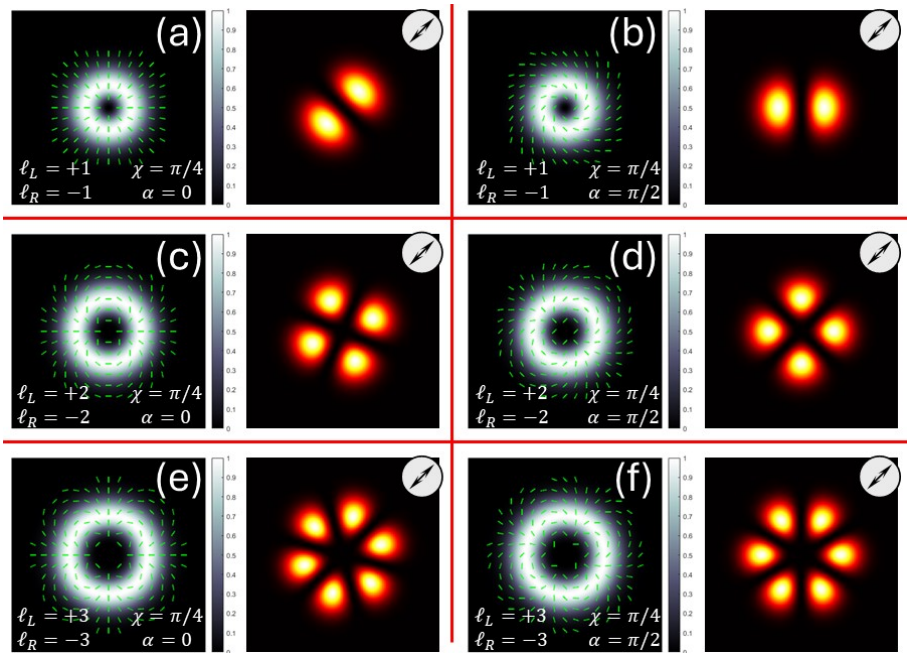

Fig. 2. Simulation examples of CVBs generated by the superposition of two LG beams encoded onto the $|\mathbf{R}\rangle$ and $|\mathbf{L}\rangle$ states.

3. Adaptive spiral phase plate and the compound AQ-plate

The core element in the compound AQ-plate is the recently developed LC adaptive spiral phase plate (ASPP) [35]. The ASPP is a LC device that employs the transmission electrode technique and patterned electrodes to generate controllable spiral phase profiles by inducing an azimuthal

Optics EXPRESS

voltage distribution in the active area. The device consists of two ITO-coated glass substrates separated by a 50μm spacer, where now the cavity is filled with the nematic LC HTD028200-200 [43] having birefringence $\Delta n = 0.27$ for the wavelength $\lambda = 633\ nm$. One substrate consists of a photolithographically-patterned circular transmission electrode connected to voltage sources V1 and V2 and an array of 100 "pie-slice" ITO electrodes that distribute the voltage almost uniformly across the active area (Fig. 3(a)). By adjusting the applied voltages, the ASPP can dynamically generate both positive and negative tunable topological charges. The operating voltage range is selected to ensure linearity in the LC's birefringence response, which is essential for producing the spiral phase profiles.

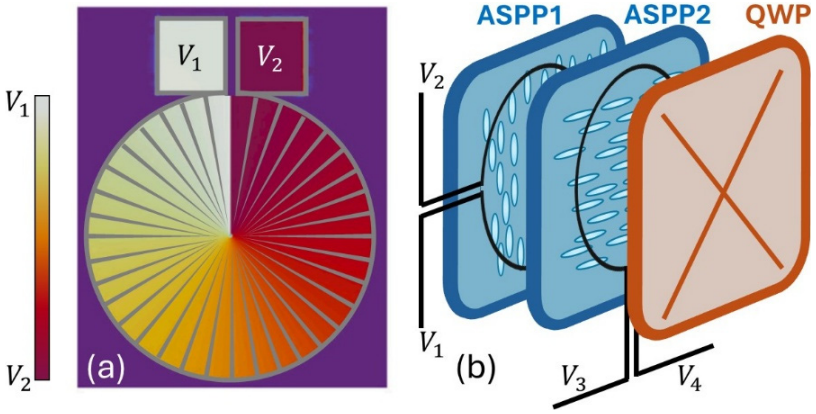

Fig. 3. (a) Schematic depiction of the circular transmission electrode with ITO slices evenly arranged to distribute the voltage (drawings are not to scale, the space between adjacent slices is about 10 μm). (b) Scheme of the tunable LC-plate.

Figure 3(b) shows a scheme of the compound adaptive q-plate. It consists of two ASPPs with perpendicular orientation, followed by a quarter-wave plate (QWP) with neutral axes at 45° relative to the axes of the SPP layers. The first adaptive plate (ASPP1) has its LC director aligned in the vertical direction, thus encoding a spiral phase of topological charge ℓ_1 onto the vertical linear polarization component of the input beam. Because the horizontal polarization component is aligned with the LC ordinary index, it is not affected by the voltage applied to this layer. The second plate (ASPP2) is oriented with its LC director aligned horizontal. Now the horizontal polarization component is affected by the spiral phase of topological charge ℓ_2, leaving the vertical polarization unmodulated. This way, a CVB is readily generated.

However, to produce the standard CVBs as those shown in Fig. 2, with constant ellipticity but azimuthal variation of its orientation, the spiral phases must be encoded on the circular polarization components. This is achieved by adding a QWP with neutral axes oriented at 45° relative to the LC director of the ASPPs, to transform the vertical/horizontal polarization states into the left/right circular states. The output vector beam can then be described with Eq. (3) by selecting the charges in SPP1 and SPP2 as the ones required for the output $|\mathbf{L}\rangle$ and $|\mathbf{R}\rangle$ components respectively, i.e., $\ell_1 = \ell_L$ and $\ell_2 = \ell_R$.

The compound AQ-plate provides a one-to-one mapping between each point of the standard PS (Fig. 1(a)) and the HOPS (Fig. 1(b)), in a similar way as standard q-plates do [39]. However, the mapping is different than that achieved with the standard q-plate. Here, input uniform polarization $|\mathbf{V}\rangle$ and $|\mathbf{H}\rangle$ linear states provide vortex outputs $e^{i\ell_L}|\mathbf{L}\rangle$ and $e^{i\ell_R}|\mathbf{R}\rangle$ respectively, and input uniform polarization $|\mathbf{D}\rangle$, $|\mathbf{A}\rangle$, $|\mathbf{R}\rangle$ and $|\mathbf{L}\rangle$ states provide linearly polarized CVBs.

Finally, another important detail that must be considered to retrieve the correct mapping that the AQ-plate performs between the standard PS and the HOPS is the orientation of the line

Optics EXPRESS

electrode that sets the origin of the spiral phase. Being ASPP2 rotated by 90° with respect to ASPP1 (Fig. 3(b)) makes their phase origin differ in 90°. Therefore, the Jones matrix of the device, $\mathbf{A_q}$, can be expressed as

$$\mathbf{A_q} = e^{i\ell_L\theta}|\mathbf{L}\rangle\langle\mathbf{V}| + ie^{i\ell_R\theta}|\mathbf{R}\rangle\langle\mathbf{H}| = \frac{1}{\sqrt{2}}\begin{pmatrix} ie^{i\ell_R\theta} & e^{i\ell_L\theta} \\ -e^{i\ell_R\theta} & -ie^{i\ell_L\theta} \end{pmatrix}, \tag{7}$$

where the i factor in the summation term in Eq. (7) accounts for the 90° phase delay between the phase origin of the two ASPP devices. Hence, with these considerations the mapping relations read:

$$|\mathbf{H}\rangle \xrightarrow{\mathbf{A_q}} ie^{-i\theta}|\mathbf{R}\rangle, \qquad |\mathbf{V}\rangle \xrightarrow{\mathbf{A_q}} e^{+i\theta}|\mathbf{L}\rangle, \tag{8a}$$

$$|\mathbf{D}\rangle \xrightarrow{\mathbf{A_q}} e^{i\pi/4}|\mathbf{Asl}\rangle, \qquad |\mathbf{A}\rangle \xrightarrow{\mathbf{A_q}} -e^{i\pi/4}|\mathbf{Sl}\rangle, \tag{8b}$$

$$|\mathbf{R}\rangle \xrightarrow{\mathbf{A_q}} i|\mathbf{Rd}\rangle, \qquad |\mathbf{L}\rangle \xrightarrow{\mathbf{A_q}} |\mathbf{Az}\rangle. \tag{8c}$$

These mapping relations can be easily obtained (except for the multiplying phase factor) as the rotations of the PS indicated in Fig. 1 by the blue arrows. This transformation path stems from the fact that the Jones matrix of the AQ-plate can be written as $\mathbf{A_q} = \mathbf{Q}\cdot\mathbf{Q_{w(-45)}}$ where $\mathbf{Q_{w(-45)}} = |\mathbf{D}\rangle\langle\mathbf{D}| + i|\mathbf{A}\rangle\langle\mathbf{A}|$ represents a QWP oriented along S2 and $\mathbf{Q}$ is the Jones matrix of the standard q-plate defined in Eq. (6). Therefore, using the latter decomposition, the AQ-plate Jones matrix can be written as $\mathbf{A_q} = \mathbf{T}\cdot\mathbf{H_w}\cdot\mathbf{Q_{w(-45)}}$. Hence, the mapping from an input state on the PS (Fig. 1(a)) to a state on the HOPS (Fig. 1(b)) involves first a 90° rotation around the S2 axis (Fig. 1(c)), followed by a 180° rotation around the S1 axis (Fig. 1(d)) and finally the direct mapping to the HOPS. To clearly illustrate it, three symbols (triangle, square and circle) drawn on the PS in Fig. 1(a) show three input polarizations, $|\mathbf{R}\rangle$, $|\mathbf{H}\rangle$ and $|\mathbf{D}\rangle$ respectively. The transformations performed by the AQ-plate (blue symbols) as compared to the action of the standard q-plate (green symbols) and the azimuthal polarization rotator (red symbols) on these three different input states are indicated with the corresponding coloured symbol in the HOPS. For example, in the case of the AQ-plate, the input $|\mathbf{R}\rangle$ state in sphere (a) (triangle) is transformed onto the $|\mathbf{H}\rangle$ state in sphere (c), is kept unchanged in step (d) since it lies along the rotation axis S1 and is finally directly mapped onto the radial state in sphere (b). Likewise, the input $|\mathbf{H}\rangle$ state in sphere (a) (square) is transformed onto the $|\mathbf{L}\rangle$ state in sphere (c), it then yields the $|\mathbf{R}\rangle$ state because of the 180° rotation around the S1 axis and is finally directly mapped onto the $|\mathbf{R}\rangle$ vortex on the HOPS in (b). Similarly, the anti-slanted state (blue circle in Fig. 1(b)) results from operating the AQ-plate on the input diagonal state on the PS, Fig. 1(a).

4. Experimental results

4.1. Verification of the spiral phase generation

As a first step to assess the performance of the compound AQ-plate, the generation of tunable optical vortices by plates ASPP1 and ASPP2 was examined. Following the procedure described in [35] and sketched in Fig. 4(a), each device was placed between crossed polarizers (P1 and P2) oriented at 45° with respect to the LC director and then imaged onto a camera. This image shows an azimuthal intensity variation, as shown in the inset of Fig. 4(b) for cases $\ell = 3$ and $\ell = 4$. From this intensity variation the azimuthal phase variation was retrieved. In each case one of the voltage sources (V1 or V2 in Fig. 3(a)) was kept constant while the other was varied until the expected azimuthal intensity pattern was observed, with equally spaced dark radial lines. The graph in Fig. 4(b) shows the voltages required in the electrode with variable voltage to achieve the corresponding topological charge. In order to generate topological charges $\pm\ell$, ranging from 1 to 13, voltages V1 and V2 were adjusted accordingly. Fractional charges can be applied as

Optics EXPRESS

well by using the intermediate voltages. For positive ℓ, V1 varied within the range from 1.38 Vrms to 2.44 Vrms, while V2 was held constant at 1.3 Vrms. By reversing V1 and V2, a negative spiral phase is produced with practically the same voltages, and the corresponding images feature dark lobes rotating in the opposite sense (as shown in Fig. 5 of Ref. [35]). The procedure was repeated for both ASPPs, concluding that very similar voltage values were required in each plate to obtain the same charges, as shown in Fig. 4(b).

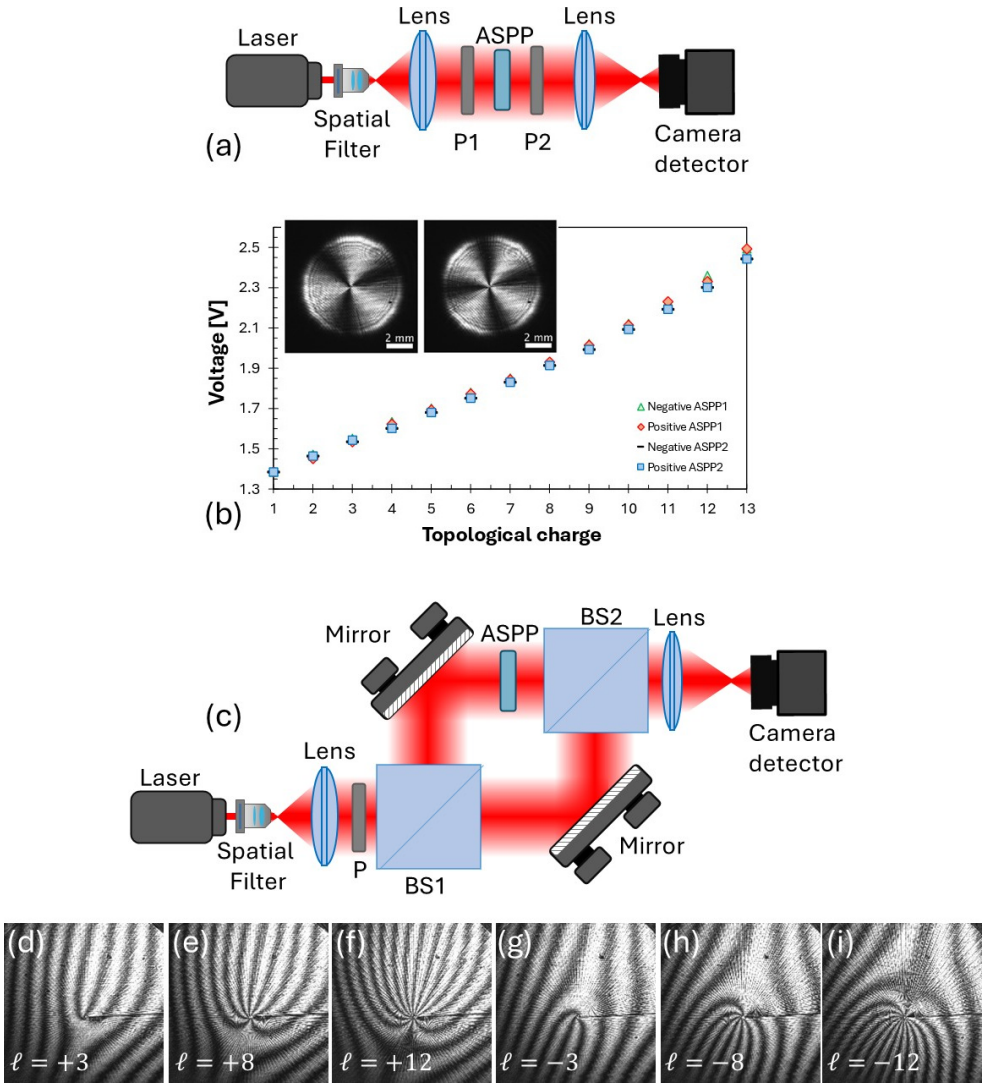

Fig. 4. (a) Scheme of the optical system to measure the ASPP retardance by imaging it between crossed linear polarizers (P1 and P2). (b) Voltages required to achieve a given topological charge from $\ell = \pm 1$ to ± 13. One electrode is kept constant at 1.3 Vrms while changing the voltage on the other electrode. The inset shows an ASPP image for $\ell = 3$ and $\ell = 4$. (c) Optical interferometer for verifying the sign of the spiral phase. (d)-(i) Experimental interferograms for $\ell = \pm 3$, $\ell = \pm 8$ and $\ell = \pm 12$.

However, these intensity images do not reveal the sign of the charge as clearly as interference patterns do, particularly for high-enough charge values, where the different sense of rotation of the dark lobes is less noticeable. Therefore, to confirm the successful generation of spiral phases

Optics EXPRESS

more conclusively, each device was placed in one of the arms of a March-Zehnder interferometer, as in Fig. 4(c). The input polarizer (P) is oriented parallel to the LC director axis. Again, a lens was used to image the ASPP plane onto a camera that recorded the interferograms where the spiral phase can be visualized as a fork-like pattern

Voltages were adjusted to produce a spiral phase with charges $\ell = \pm 3,\ \pm 8$ and ± 12. Figure 4(d-i) illustrates the interferograms for one of the ASPPs. The charge value is clearly visible in the number of fringes where the central fringe splits at the singularity. Upon reversing the voltage, the spiral phase rotates in opposite sense, and the topological charge changes sign. This is clearly revealed by the reversal of the orientation (upward or downward) of the fork interference pattern. The interferograms in Fig. 4 disclose the electrode pattern described in Section 3 since the camera is imaging the ASPP plane. Notably, a horizontal dark line appears in the right half of each interferogram, along with fainter radial lines corresponding to the electrode structure. This horizontal line arises from the proximity of the two control electrodes in that region, causing an abrupt change in the applied voltage. The voltage discontinuity results in a phase discontinuity that manifests itself as a dark horizontal line in the intensity pattern captured by the camera.

This voltage gap between the two control electrodes (V1 and V2) limits the maximum achievable topological charge, since higher topological charges require a larger voltage gap in order to fit more 2π cycles in a single roundtrip. On the other hand, an excessive voltage gap value makes the LC enter the non-linear zone of its birefringence curve [35]. As mentioned, the ASPP must be operated within the linear birefringence zone to ensure a phase variation linear with the azimuth. Therefore, the highest achievable topological charge is the result of a tradeoff which, for these ASPPs based on commercial nematic liquid crystal HTD028200-200 having a birefringence $\Delta n = 0.2719$ at $\lambda = 633$ nm, leads to $\ell = 13$. Of course, using a LC material with higher birefringence and/or linear response within a broader voltage range would provide higher topological charges. In addition, as revealed by the faint radial lines in the interferograms, the azimuthal voltage distribution is not perfectly continuous, because of the 10 μm separation between adjacent "pie-slice" ITO electrodes. As recently reported [44], this can be overcome by coating the active area with a high-resistivity layer of a conducting polymer, thus filling the spacing between the ITO electrodes and yielding a completely continuous voltage distribution.

Despite these electrode-induced features in the ASPP image plane, the experimental results discussed in the following sections demonstrate that they do not significantly affect the quality of the CVBs generated in the far field. Thus, the abrupt phase change, caused by the voltage gap in the two control electrodes, is confined to a region that minimally influences the overall beam-shaping performance of the device.

4.2. Experimental generation of pure CVBs

In this subsection we present experimental results that confirm the effective realization of pure CVBs using the AQ-plate device. The CVB was focused by means of a convergent lens and a camera was placed in the focal plane. Figure 5 shows the far-field captures of the generated first-order CVBs. The AQ-plate was illuminated with the six standard polarization states: linear states $|\mathbf{H}\rangle$, $|\mathbf{V}\rangle$, $|\mathbf{D}\rangle$, and $|\mathbf{A}\rangle$, and circular states $|\mathbf{R}\rangle$ and $|\mathbf{L}\rangle$ (each row in Fig. 5 corresponds to one input state). For every input state, the beam was captured without analyzer (1st column) and then with a polarization analyzer located in front of the camera, set to transmit the six cardinal states. This was done by simply rotating the linear polarizer, and by adding a QWP when detecting the circular components.

On the other hand, when illuminating the AQ-plate with input states $|\mathbf{D}\rangle$, $|\mathbf{A}\rangle$, $|\mathbf{R}\rangle$ and $|\mathbf{L}\rangle$ we obtain the first-order linear CVBs lying in the equator of the first-order HOPS of Fig. 1(b). For instance, input state $|\mathbf{R}\rangle$ yields the radial polarization. This is noticed by the position of the two lobes in the image captures, which rotate following the analyzer rotation. Similarly, one can verify that input state $|\mathbf{L}\rangle$ leads to the azimuthal polarization output, and input states $|\mathbf{D}\rangle$ and

Optics EXPRESS

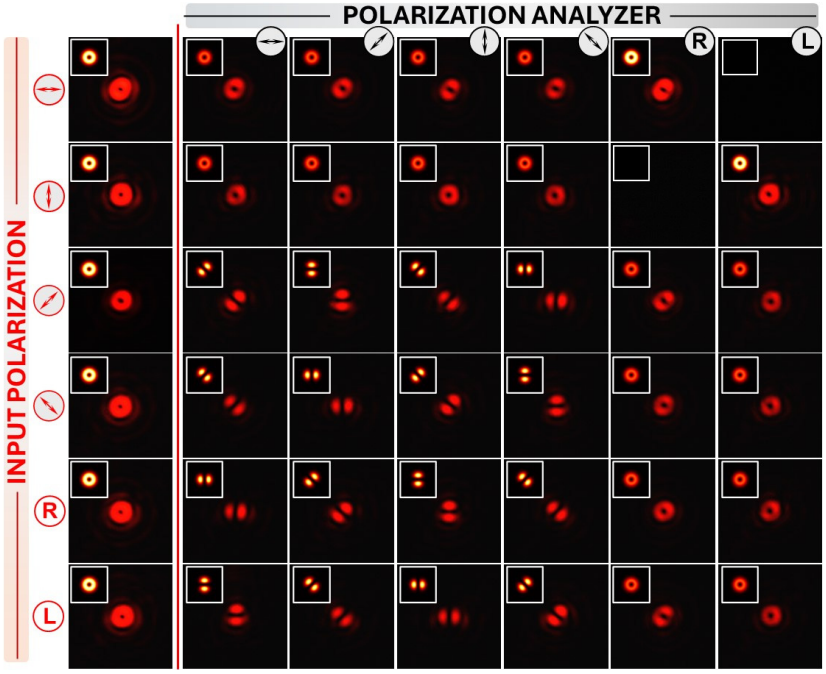

Fig. 5. Experimental verification of the generation of vector beams with charges $\ell_L = +1$ and $\ell_R = -1$. The left column shows the intensity capture without analyzer. The inset in each case shows computer simulations of the intensity pattern.

$|\mathbf{A}\rangle$ provide the anti-slanted and the slanted states. In all cases the mapping relations of Eq. (8), regarding the output polarization state, are verified. Furthermore, the experimental results in Fig. 5 assess the good quality of the CVBs generated by the AQ-plate. This is concluded when comparing to the numerical simulations presented in the inset of every captured image.

To probe the tunability of the AQ-plate in terms of the topological charge, now the CVBs of the second-order HOPS are generated. This is achieved by applying higher voltages to ASPP1 and ASPP2 to obtain $\ell_1 = \ell_L = +2$ and $\ell_2 = \ell_R = -2$. In this case the rms voltages are V1 = 1.3, V2 = 1.46 and V3 = 1.46, V4 = 1.3 volts respectively.

The results in Fig. 6 show the same behaviour as those in Fig. 5, except for two important differences: i) the diameter of the circular doughnut beam when no analyzer is included is now larger than in Fig. 5, and ii) the number of lobes in the linearly polarized CVBs is now four. Again, the experimental captures agree very well with the expected intensity patterns plotted in the insets.

These results in Figs. 5 and 6 prove the successful generation of pure CVBs of first and second order. However, as shown in Fig. 4, the ASPPs plates can produce with good quality arbitrary charges up to 12. Therefore, we have tested the possibility of generating pure CVBs of such high order. The results are presented in Fig. 7 for cases with $\ell_L = -\ell_R = 0,\ 1,\ 2,\ 3,\ 6,\ 8,\ 10$ and 12. We only plot the intensity patterns where the input state is $|\mathbf{R}\rangle$, without analyzer and through a diagonal linear analyzer. As it is shown, the diameter of the doughnut beam increases with the topological charge, and more importantly, the number of lobes is always twice the encoded charge. Again, the numerical calculations (insets) agree very well with the experiments.

Optics EXPRESS

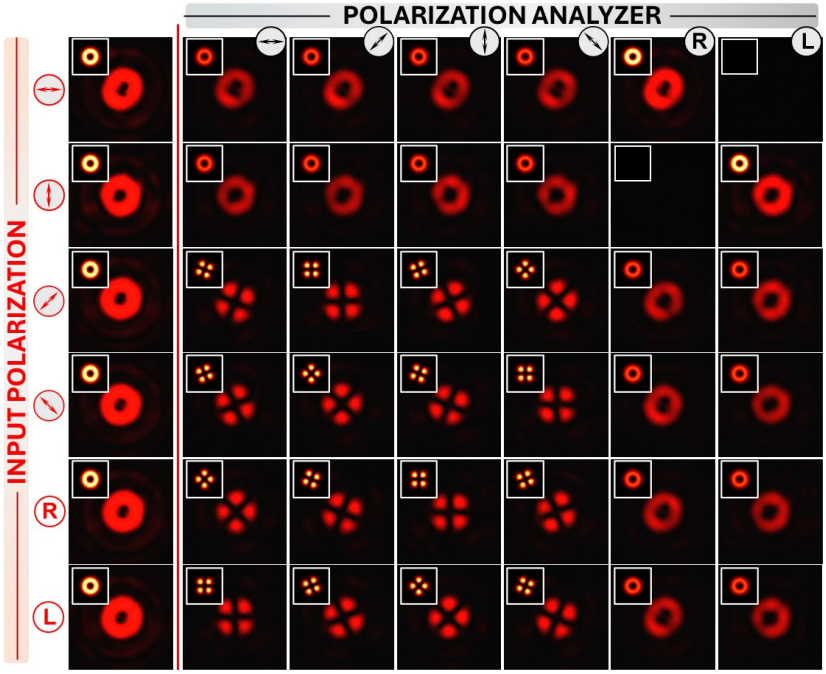

Fig. 6. Experimental verification of the generation of vector beams with charges $\ell_L = +2$ and $\ell_R = -2$. The left column shows the intensity capture without analyzer. The inset in each case shows computer simulations of the intensity pattern.

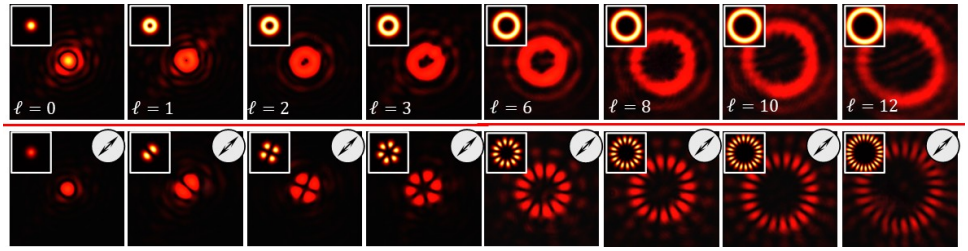

Fig. 7. Experimental generation of pure vector beams with charges $\ell_L = -\ell_R = \ell$ with different charges ℓ up to 12. The input beam is polarized as an $|\mathbf{R}\rangle$ state. For each case the top image is the capture without analyzer while the bottom image is the beam filtered through a linear diagonal analyzer.

4.3. Experimental generation of hybrid CVBs

The results in the previous subsection only consider the generation of pure CVBs, which are obtained when $\ell_L = -\ell_R$. However, the AQ-plate is not restricted to this situation (unlike standard q-plates), since an independent charge can be addressed to each ASPP. Therefore, the AQ-plate device can be set to generate hybrid CVBs, as we demonstrate in Fig. 8 and Fig. 9. Since the beam's diameter changes with the charge, we selected charge values close enough to provide a good overlap of the two vortex beam circular components.

Figure 8 take as starting point the pure CVB obtained with $\ell_L = -\ell_R = 6$. The input polarization state is once again $|\mathbf{R}\rangle$. Figure 8(a) -first column- shows the expected intensity and polarization map obtained through numerical simulations, which features local linear polarization at all points (depicted as green in the figure). The numerical calculation of the intensity transmitted

Optics EXPRESS

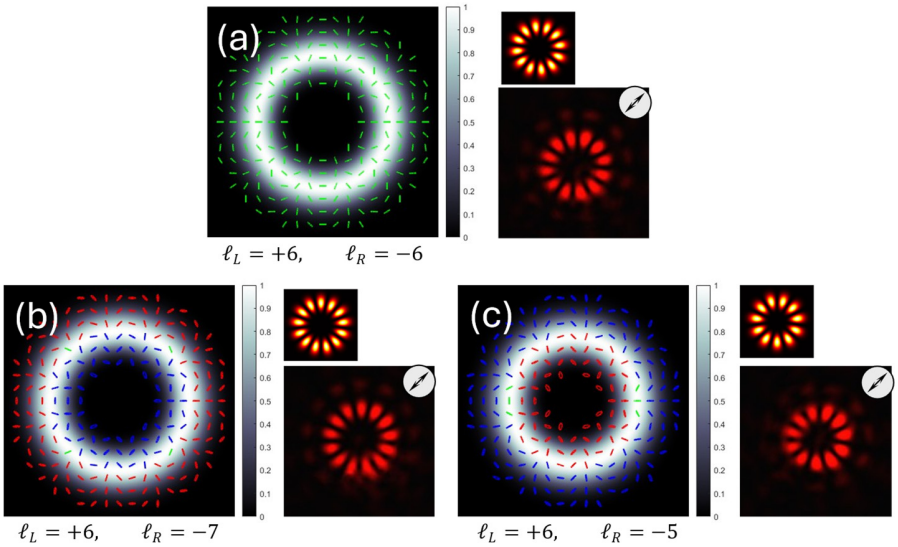

Fig. 8. Simulated intensity and polarization pattern for: (a) a pure vector beam with charges $\ell_L = -\ell_R = 6$, and hybrid vector beams with charges (b) $\ell_R = +6$ and $\ell_L = -7$ and (c) $\ell_R = +6$ and $\ell_L = -5$. The input beam is polarized as an $|\mathbf{R}\rangle$ state. In each case the second column shows the intensity transmitted through a diagonal linear analyzer, with numerical simulations (top) and the corresponding experimental capture (bottom).

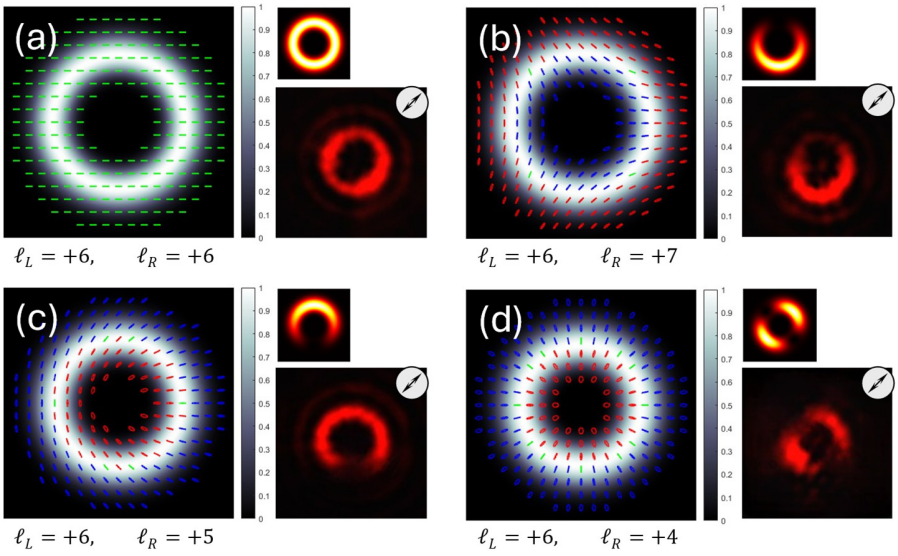

Fig. 9. Simulated intensity and polarization pattern for: (a) a pure vector beam with charges $\ell_L = \ell_R = +6$, and hybrid vector beams with charges (b) $\ell_R = +6$ and $\ell_L = +7$, (c) $\ell_R = +6$ and $\ell_L = +5$ and (d) $\ell_L = +6$ and $\ell_R = +4$. The input beam is polarized as an $|\mathbf{R}\rangle$ state. In each case the second column shows the intensity transmitted through a diagonal linear analyzer, with numerical simulations (top) and the corresponding experimental capture (bottom).

through a diagonal linear analyzer is plotted in the second column of Fig. 8(a) together with the experimental capture, revealing a very good agreement and the expected $|\ell_L - \ell_R| = 12$ lobes.

Optics EXPRESS

Figures 8(b) and 8(c) present the corresponding numerical and experimental results for $\ell_L = +6$ and $\ell_R = -7$, and $\ell_L = +6$ and $\ell_R = -5$ respectively. Now, in Fig. 8(b) the outer part of the doughnut beam shows right helicity (indicated as red ellipses), while the inner part of the circle shows left helicity (indicated as blue ellipses). This occurs because $|\ell_R|>|\ell_L|$ and therefore the diameter of the focused doughnut beam in the $|\mathbf{R}\rangle$ component is larger than the one in the $|\mathbf{L}\rangle$ component. The situation is reversed in Fig. 8(c), since now $|\ell_L|>|\ell_R|$. Hence, the inner part of the circle has right helicity while the outer part shows left helicity. Nevertheless, in both cases the ellipticity is very low. The difference between cases is much easier to note by placing a linear analyzer and counting the number of lobes. In Fig. 8(b) we find $|\ell_L - \ell_R| = 13$ lobes while in Fig. 8(c) there are $|\ell_L - \ell_R| = 11$ lobes.

Figure 9(a) considers a similar situation, with input $|\mathbf{R}\rangle$ polarization and diagonal linear analyzer, but taking as a starting point the case with $\ell_L = \ell_R = +6$, i.e. now both polarization components encode the same charge. Therefore, the output is a vortex beam of uniform polarization. This provides a doughnut beam when observed without analyzer (first column) and also when placing the diagonal linear analyzer (second column). In Fig. 9(b) the addressed voltages are those to yield charges $\ell_L = +6$ and $\ell_R = +7$. The intensity pattern without analyzer is equivalent to that in Fig. 8(b), with again the outer part of the ring featuring right helicity while the inner part shows left helicity. But the most significant difference with respect to the case in Fig. 8(b) is that now these charge values lead to $|\ell_L - \ell_R| = 1$. Consequently, only one single lobe that adopts the shape of a half-moon is expected when transmitting the beam through the linear analyzer. This is indeed shown in the numerical simulation as well as in the experimental result plotted in the second column of Fig. 9(b).

Figures 9(c) and 9(d) illustrate the cases with charges $\ell_L = +6$ and $\ell_R = +5$, and $\ell_L = +6$ and $\ell_R = +4$ respectively. In both situations the outer part of the ring has left helicity while the inner part has right helicity. Figure 9(c) shows an intensity pattern through the diagonal linear analyzer like that in Fig. 9(b), i.e., with a single lobe (again the difference $|\ell_L - \ell_R|$ is one), but now the bright lobe is pointing upward instead of downward. In Fig. 9(d) the difference is $|\ell_L - \ell_R| = 2$, thus two lobes are observed behind the analyzer. The experiments confirm the result in all cases.

5. Conclusions

In summary, we have presented the proof-of-concept of a new LC device that enables the dynamic generation of arbitrary CVBs, with tunability both in the operation wavelength and in the topological charge. The proposed device consists of two LC ASPP cascaded with a quarter-wave plate layer. A specially designed electrode distribution allows to independently tune the topological charge in each spiral phase plate, which are encoded in the output circular polarization components. Because the topological charges can be controlled independently, the device can generate arbitrary CVBs. The LC employed in this device (HTD028200-200) operates in the visible range and has a moderate birefringence ($\Delta n = 0.2716$ at 633 nm). Thus, it is useful to generate tunable CVB in the visible range, once the required voltages have been calibrated, since the retardance of each layer depends on the wavelength. The device shows the remarkable advantage of encoding independent and tunable topological charges in each output circular polarization component. This proof-of-concept device could be further improved by refining the design of the constituent ASPP using the recently reported trans-modal technique [44]. Employing a LC material with higher birefringence, such as the mixture NLC1929 ($\Delta n = 0.3375$ at 633 nm) [45] could further improve its performance. Compared to SLMs, the proposed device is compact, transmissive, and with an electrode design advantageous for generating CVBs without significant diffraction losses. The presented proof-of-concept AQ-plate remains comparable in size to SLMs. However, it has the potential to be scaled to more compact integrated devices for generating reconfigurable structured light, a field where the integration of liquid-crystals with

Optics EXPRESS

metasurfaces is one of the mechanisms to achieve tunability of the different degrees of freedom [46,47].

Funding. Ministerio de Ciencia, Innovación y Universidades (PID2021-126509OB-C22, PID2022-137269OB-C22, RYC2022-035279-I, PDC2022-133332-C22); Generalitat Valenciana (CIBEST/2023/119); Wojskowa Akademia Techniczna (UGB 531-000031-W900-22).

Disclosures. The authors declare no conflicts of interest.

Data availability. Data underlying the results presented in this paper may be available from the corresponding author upon reasonable request.

References

1. Q. Zhan, "Cylindrical vector beams: From mathematical concepts to applications," Adv. Opt. Photonics **1**(1), 1–57 (2009).
2. A. Kritzinger, A. Forbes, and P. B. C. Forbes, "Optical trapping and fluorescence control with vectorial structured light," Sci. Rep. **12**(1), 17690 (2022).
3. E. Otte, C. Alpmann, and C. Denz, "Polarization singularity explosions in tailored light fields," Laser Photonics Rev. **12**(6), 1700200 (2018).
4. V. Curcio, L. A. Alemán-Castañeda, T. G. Brown, *et al.*, "Birefringent Fourier filtering for single molecule coordinate and height super-resolution imaging with dithering and orientation," Nat. Commun. **11**(1), 5307 (2020).
5. B. Ndagano, I. Nape, M. A. Cox, *et al.*, "Creation and detection of vector vortex modes for classical and quantum communication," J. Lightwave Technol. **36**(2), 292–301 (2018).
6. C. Maurer, A. Jesacher, S. Fürhapter, *et al.*, "Tailoring of arbitrary optical vector beams," New J. Phys. **9**(3), 78 (2007).
7. P. García-Martínez, D. Marco, J. L. Martínez-Fuentes, *et al.*, "Efficient on-axis SLM engineering of optical vector modes," Opt. Lasers Eng. **125**, 105859 (2020).
8. I. Moreno, J. A. Davis, K. Badham, *et al.*, "Vector beam polarization state spectrum analyzer," Sci. Rep. **7**(1), 2216 (2017).
9. M. Stalder and M. Schadt, "Linearly polarized light with axial symmetry generated by liquid-crystal polarization converters," Opt. Lett. **21**(23), 1948–1950 (1996).
10. J. M. Otón, J. Pereiro-García, X. Quintana, *et al.*, "Optimizing tunable LC devices with twisted light," Crystals **14**(1), 16 (2023).
11. N. Hashimoto and K. Ogawa, "Liquid crystal Laguerre-Gaussian vector beam generator and its applications," Mol. Cryst. Liq. Cryst. **768**(10), 327–343 (2024).
12. M. Beresna, M. Gecevičius, P. G. Kazansky, *et al.*, "Radially polarized optical vortex converter created by femtosecond laser nanostructuring of glass," Appl. Phys. Lett. **98**(20), 201101 (2011).
13. P. Zhang, Q. Wang, T. Zhao, *et al.*, "Generation of vortex beams via all-dielectric spin-multiplexed coding metamaterials," J. Lightwave Technol. **41**(23), 7148–7154 (2023).
14. J. Jia, K. Zhang, G. Hu, *et al.*, "Arbitrary cylindrical vector beam generation enabled by polarization-selective Gouy phase shifter," Photonics Res. **9**(6), 1048–1054 (2021).
15. L. Marrucci, C. Manzo, and D. Paparo, "Optical spin-to-orbital angular momentum conversion in inhomogeneous anisotropic media," Phys. Rev. Lett. **96**(16), 163905 (2006).
16. A. Rubano, F. Cardano, B. Piccirillo, *et al.*, "Q-plate technology: a progress review," J. Opt. Soc. Am. B **36**(5), D70–D87 (2019).
17. K. K. Anoop, A. Rubano, R. Fittipaldi, *et al.*, "Femtosecond laser surface structuring of silicon using optical vortex beams generated by a q-plate," Appl. Phys. Lett. **104**(24), 241604 (2014).
18. C. Loussert, K. Kushnir, and E. Brasselet, "Q-plates micro-arrays for parallel processing of the photon orbital angular momentum," Appl. Phys. Lett. **105**(12), 121108 (2014).
19. G. Milione, M. P. J. Lavery, H. Huang, *et al.*, "4×20 Gbit/s mode division multiplexing over free space using vector modes and a q-plate mode (de)multiplexer," Opt. Lett. **40**(9), 1980–1983 (2015).
20. W. Shu, X. Ling, X. Fu, *et al.*, "Polarization evolution of vector beams generated by q-plates," Photonics Res. **5**(2), 64–72 (2017).
21. D. Naidoo, F. S. Roux, A. Dudley, *et al.*, "Controlled generation of higher-order Poincaré sphere beams from a laser," Nat. Photonics **10**(5), 327–332 (2016).
22. S. Slussarenko, A. Murauski, T. Du, *et al.*, "Tunable liquid crystal q-plates with arbitrary topological charge," Opt. Express **19**(5), 4085–4090 (2011).
23. J. A. Davis, N. Hashimoto, M. Kurihara, *et al.*, "Analysis of a segmented q-plate tunable retarder for the generation of first-order vector beams," Appl. Opt. **54**(32), 9583–9590 (2015).
24. J. C. Quiceno-Moreno, D. Marco, M. M. Sánchez-López, *et al.*, "Analysis of hybrid vector beams generated with a detuned q-plate," Appl. Sci. **10**(10), 3427 (2020).
25. M. M. Sánchez-López, I. Abella, D. Puerto-García, *et al.*, "Spectral performance of a zero-order liquid-crystal polymer commercial q-plate for the generation of vector beams at different wavelengths," Opt. Laser Technol. **106**, 168–176 (2018).

Optics EXPRESS

26. E. E. James, I. M. Anderson, and D. A. Gregory, "Spectropolarimetric properties of vortex retarders," Opt. Express **32**(17), 30124–30143 (2024).
27. G. Milione, H. I. Sztul, D. A. Nolan, *et al.*, "Higher-order Poincaré sphere, Stokes parameters, and the angular momentum of light," Phys. Rev. Lett. **107**(5), 053601 (2011).
28. S. Chen, X. Zhou, Y. Liu, *et al.*, "Generation of arbitrary cylindrical vector beams on the higher order Poincaré sphere," Opt. Lett. **39**(18), 5274–5276 (2014).
29. A. M. Beckley, T. G. Brown, and M. A. Alonso, "Full Poincaré beams," Opt. Express **18**(10), 10777–10785 (2010).
30. J. C. Suárez-Bermejo, J. C. G. de Sande, M. Santarsiero, *et al.*, "Mueller matrix polarimetry using full Poincaré beams," Opt. Laser Eng. **122**, 134–141 (2019).
31. R. C. Devlin, A. Ambrosio, N. A. Rubin, *et al.*, "Arbitrary spin–to–orbital angular momentum conversion of light," Science **358**(6365), 896–901 (2017).
32. Y.-W. Huang, N. A. Rubin, A. Ambrosio, *et al.*, "Versatile total angular momentum generation using cascaded J-plates," Opt. Express **27**(5), 7469–7484 (2019).
33. E. J. Galvez, S. Khadka, W. H. Schubert, *et al.*, "Poincaré-beam patterns produced by nonseparable superpositions of Laguerre-Gauss and polarization modes of light," Appl. Opt. **51**(15), 2925–2934 (2012).
34. M. M. Sánchez-López, J. A. Davis, I. Moreno, *et al.*, "Gouy phase effects on propagation of pure and hybrid vector beams," Opt. Express **27**(3), 2374–2386 (2019).
35. T. Jankowski, N. Bennis, P. Morawiak, *et al.*, "Optical vortices by an adaptive spiral phase plate," Opt. Laser Technol. **176**, 111029 (2024).
36. K. Yoshiki, K. Ryosuke, M. Hashimoto, *et al.*, "Second-harmonic generation microscope using eight-segment polarization-mode converter to observe three-dimensional molecular orientation," Opt. Lett. **32**(16), 2465 (2007).
37. M. Caño-García, X. Quintana, J. M. Otón, *et al.*, "Dynamic multilevel spiral phase plate generator," Sci. Rep. **8**(1), 15804 (2018).
38. S. Delaney, M. M. Sánchez-López, I. Moreno, *et al.*, "Arithmethic with q-plates," Appl. Opt. **56**(3), 596–600 (2017).
39. F. Cardano, E. Karimi, S. Slussarenko, *et al.*, "Polarization pattern of vector vortex beams generated by q-plates with different topological charges," Appl. Opt. **51**(10), C1–C6 (2012).
40. I. A. Litvin, S. Ngcobo, D. Naidoo, *et al.*, "Doughnut laser beam as an incoherent superposition of two petal beams," Opt. Lett. **39**(3), 704–707 (2014).
41. M. J. Padgett and J. Courtial, "Poincaré-sphere equivalent for light beams containing orbital angular momentum," Opt. Lett. **24**(7), 430–432 (1999).
42. D. Marco, M. M. Sánchez-López, C. Hernández-García, *et al.*, "Extending the degree of polarization concept to higher-order and orbital angular momentum Poincaré spheres," J. Opt. **24**(12), 124003 (2022).
43. R. Chen, Y. Huang, J. Li, *et al.*, "High-frame-rate liquid crystal phase modulator for augmented reality displays," Liq. Cryst. **46**(2), 309–315 (2019).
44. A. Walewska, N. Bennis, T. Jankowski, *et al.*, "A hybrid trans-modal liquid crystal optical vortex generator," Opt. Laser Technol. **181**, 111849 (2025).
45. N. Bennis, T. Jankowski, O. Strzezysz, *et al.*, "A high birefringence liquid crystal for lenses with large aperture," Sci. Rep. **12**(1), 14603 (2022).
46. A. H. Dorrah and F. Capasso, "Tunable structured light with flat optics," Science **376**(6591), eabi6860 (2022).
47. L. Zhou, T. Zhong, Y. Liu, *et al.*, "When structured light encounters liquid crystals," Adv. Funct. Mater. **34**(42), 240414 (2024).